CHEMISTRY

Ir-Sn pair-site triggers key oxygen radical intermediate for efficient acidic water oxidation

Xiaobo Zheng[1]†, Jiarui Yang[1]†, Peng Li[2], Qishun Wang[1], Jiabin Wu[1], Erhuan Zhang[1], Shenghua Chen[1], Zechao Zhuang[1], Weihong Lai[3], Shixue Dou[4], Wenping Sun[5]*, Dingsheng Wang[1]*, Yadong Li[1,6,7]*

The anode corrosion induced by the harsh acidic and oxidative environment greatly restricts the lifespan of catalysts. Here, we propose an antioxidation strategy to mitigate Ir dissolution by triggering strong electronic interaction via elaborately constructing a heterostructured Ir-Sn pair-site catalyst. The formation of Ir-Sn dual-site at the heterointerface and the resulting strong electronic interactions considerably reduce *d*-band holes of Ir species during both the synthesis and the oxygen evolution reaction processes and suppress their overoxidation, enabling the catalyst with substantially boosted corrosion resistance. Consequently, the optimized catalyst exhibits a high mass activity of 4.4 A mg_{Ir}^{-1} at an overpotential of 320 mV and outstanding long-term stability. A proton-exchange-membrane water electrolyzer using this catalyst delivers a current density of 2 A cm^{-2} at 1.711 V and low degradation in an accelerated aging test. Theoretical calculations unravel that the oxygen radicals induced by the π* interaction between Ir 5*d*-O 2*p* might be responsible for the boosted activity and durability.

INTRODUCTION

Oxygen electrocatalysis plays a critical role in sustainable energy devices such as water electrolyzers and metal-air batteries to accomplish energy conversion and storage (*1*–*6*). The proton-exchange-membrane water electrolyzers (PEMWE) have been considered to represent one of the most promising techniques to acquire large-scale green hydrogen due to their unique merits, featuring high current density, H_2 purity (> 99.99%), and fast dynamic response (*7*–*11*). Nevertheless, it remains a huge scientific challenge to realize superior activity and long-term stability simultaneously due to the inherently sluggish oxygen evolution reaction (OER) kinetics and the inferior corrosion resistance of catalysts in acidic media, especially at high oxidation potential (*12*–*18*).

Iridium-based catalysts have been regarded as the benchmark catalysts for the acidic OER due to their decent activity and stability, but their scarcity and dissolution issue in the high anodic potential (>1.6 V) greatly limit their large-scale practical applications (*19*–*24*). Therefore, it is highly desirable to rationally construct an advanced Ir-based catalyst that features both outstanding activity and long calendar life. Previous studies have shown that the lower oxidized state of iridium can exhibit enhanced corrosion resistance and inherent oxygen-catalyzing capability, and Sn-based metal oxides tend to be seriously corrosion-resistant even in highly oxidizing and acidic environments (*25*–*31*). In addition, triggering the creation of oxygen radicals on the surface of the catalyst which serves as electrophilic centers for a nucleophilic attack easily from H_2O has been regarded as an effective way to enhance the catalytic activity (*32*–*34*). As a consequence, triggering the formation of oxygen radicals by constructing a heterostructures system comprising Sn-based oxide-supported lower oxidized iridium species for the acidic OER and identifying the underlying structure-activity dependence are of vital significance.

Here, we report a heterostructured Ir-Sn pair-site catalyst (Ir-Sn PSC), consisting of metallic Ir NPs grafted onto antimony tin oxide nanocrystalline which features considerably reduced *d*-band holes, to mitigate Ir dissolution in acid water oxidation. Microscopic characterizations and operando x-ray absorption and emission spectroscopy collectively reveal the strong electronic coupling between Ir and Sn dual-atom sites, which could optimize the electronic structure of Ir and suppress its overoxidation. Density functional theory (DFT) calculations unravel that the formation of oxygen radicals derived from the π* interaction between Ir $5d_{z^2}$-O $2p_y$ and Ir $5d_{xz}$-O $2p_x$ contribute to the accelerated surface electron exchange-and-transfer capability, optimized oxygen adsorption energetics, and excellent corrosion resistance. Therefore, the Ir-Sn PSC exhibits superior OER activity and excellent long-term stability in the PEMWE.

RESULTS

Synthesis and characterization

The Ir-Sn PSC was prepared by a typical wet chemical method in ethylene glycol solution at 120°C for 3 hours. Optical images indicate that the color of the dispersion of the precursors changed from aqua to dark after the formation of the Ir-Sn PSC (fig. S1). Different Ir mass loading (10.2, 23.2, and 38.3 wt %, respectively) of Ir-Sn PSC and pure Ir nanoparticles (Ir NPs) were synthesized for comparison. To comprehensively consider the activity and Ir mass loading, we focused on the study of the structure-performance relationship of 23.2 wt % Ir-Sn PSC and marked it as Ir-Sn PSC for simplicity. The x-ray diffraction (XRD) patterns and transmission electron

[1]Department of Chemistry, Tsinghua University, Beijing 100084, China. [2]School of Science, Royal Melbourne Institute of Technology, Melbourne, VIC 3000, Australia. [3]Institute for Superconducting and Electronic Materials, Australia Institute for Innovation Material, University of Wollongong, Wollongong, NSW 2522, Australia. [4]Institute of Energy Materials Science, University of Shanghai for Science and Technology, Shanghai 200093, China. [5]School of Materials Science and Engineering, State Key Laboratory of Clean Energy Utilization, Zhejiang University, Hangzhou 310027, China. [6]College of Chemistry, Beijing Normal University, Beijing 100875, China. [7]Key Laboratory of Functional Molecular Solids, Ministry of Education, College of Chemistry and Materials Science, Anhui Normal University, Wuhu, 241002, China.
*Corresponding author. Email: wenpingsun@zju.edu.cn (W.S.); wangdingsheng@mail.tsinghua.edu.cn (D.W.); ydli@mail.tsinghua.edu.cn (Y.L.).
†These authors contributed equally to this work.

microscope (TEM) images suggest the successful formation of heterostructured Ir-Sn PSC (Fig. 1B and figs. S2 to S7). High-resolution TEM (HRTEM) images demonstrated that metallic Ir NPs have anchored on the $Sn_{0.88}Sb_{0.12}O_2$ (SSO) nanocrystallites, as evidenced by the presence of characteristic lattice facets of SSO (110) and Ir (111) (Fig. 1C). The high-angle annular dark-field (HAADF) and annular bright-field (ABF) scanning transmission electron microscope (STEM) images exhibit the existence of heterointerfaces between Ir NPs and SSO nanocrystallites as indicated in the red rectangles, where Ir atoms are connected and interacted with Sn atoms in the interfaces of Ir-Sn PSC (Fig. 1, D and E). Some other representative STEM images and the fast Fourier transform (FFT) pattern derived from Fig. 1D and the selected area electron diffraction pattern also further consolidate our knowledge of the formation of heterostructured Ir-Sn PSC (Fig. 1F and figs. S8 to S11). In addition, the STEM-EDS mapping and spectra, where EDS stands for energy dispersive spectroscopy, show the coexistence of Ir, Sn, Sb, and O elements in Ir-Sn PSC (Fig. 1G and fig. S12). For comparison, STEM analysis was also conducted on the SSO nanocrystallites and Ir NPs, indicating typical rutile crystal structure (space group P42/mnm) and cubic structure (space group Fm-3 m) for SSO and Ir NPs, respectively (figs. S13 to S15). It should be noted, however, that a relatively high content of oxygen was observed near the surface of Ir NPs, indicating the presence of abundant absorbed oxygen-related species (e.g., hydroxyl groups or surface-adsorbed oxygen) in Ir NPs (figs. S16 and S17). In addition, it is also worth mentioning that the high conductivity of SSO nanocrystallites is also an important factor for their selection as the support of Ir-Sn PSC (*30*, *35*). On the basis of the abovementioned structural analysis, the structural model of Ir-Sn PSC can be vividly illustrated as presented in Fig. 1A.

To examine the evolution of the electronic properties and coordination environment of Ir-Sn PSC, x-ray photoelectron spectroscopy (XPS) and x-ray absorption spectroscopy (XAS) were conducted. The high-resolution Ir 4f XPS spectrum demonstrates that Ir-Sn PSC features lower binding energy, with two sets of doublets at 61.1 and 64.1 eV and 61.7 and 64.7 eV, which can be

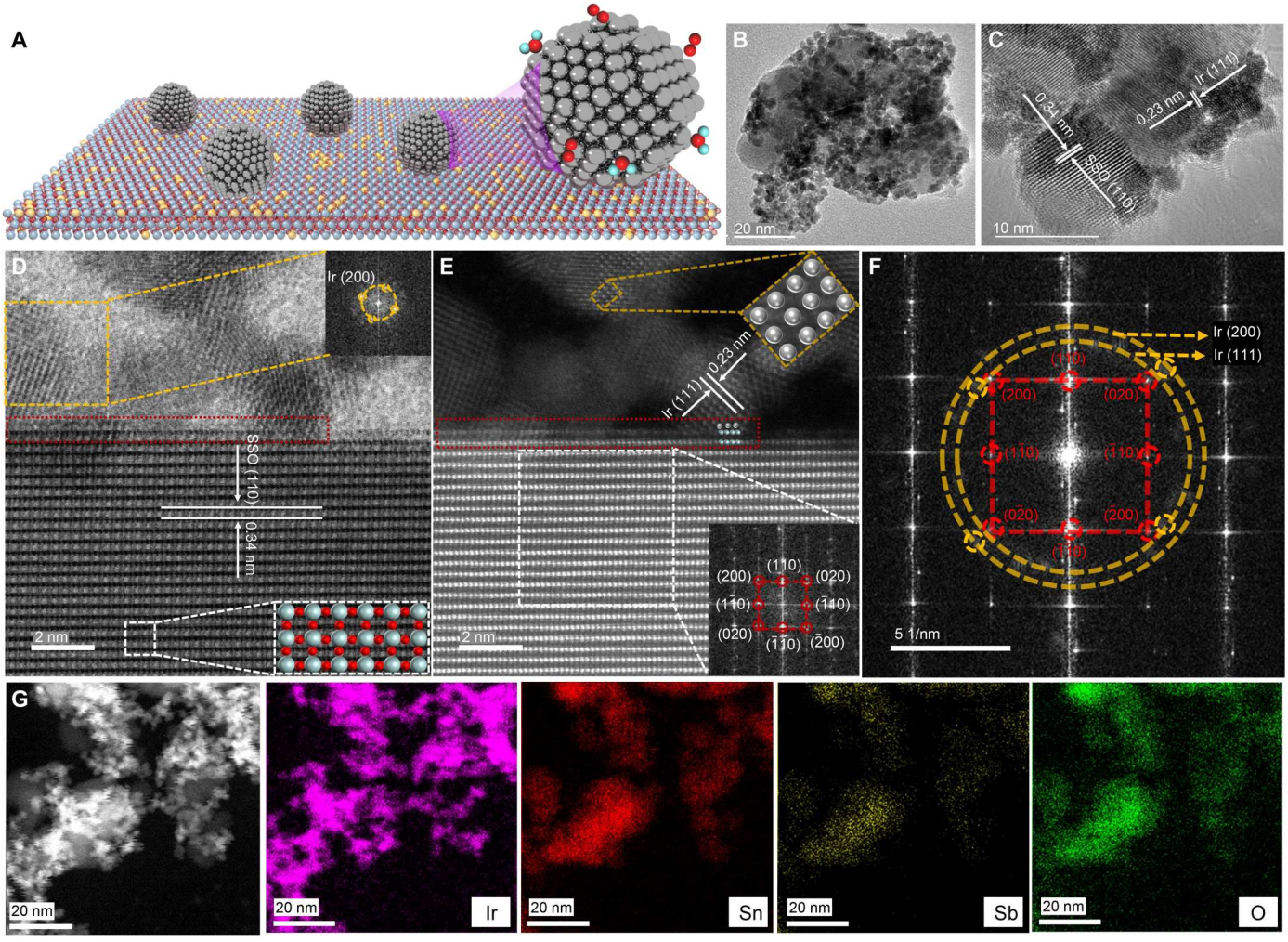

Fig. 1. The structural characterization of heterostructured Ir-Sn PSC. (**A**) Schematic illustration of Ir-Sn PSC. (**B**) TEM image. (**C**) HRTEM image. (**D**) ABF-STEM image. The top inset shows the FFT pattern of the corresponding yellow square area, and the bottom inset indicates the atomic arrangement of SSO in the white rectangle area. Red, oxygen; gray, Sn and Sb. (**E**) HAADF-STEM image, along with the FFT pattern of SSO in the white rectangle area and the atomic arrangement of Ir NPs in the yellow rectangle area. (**F**) The corresponding FFT pattern of (E). (**G**) Elemental mappings of Ir, Sn, Sb, and O in the Ir-Sn PSC.

attributed to the valence states of Ir^0 and Ir^{4+}, respectively (Fig. 2A and table S1) (*36*–*38*). In contrast, the Ir $4f_{7/2}$ and Ir $4f_{5/2}$ XPS spectrum of Ir NPs are located at higher binding energy, and the relative ratio of Ir^0/Ir^{4+} (0.17) is much lower than Ir-Sn PSC (1.2), illustrating the higher degree of surface oxidation of Ir NPs due to the absorption of oxygen species such as hydroxyl groups (Ir-OH) and adsorbed H_2O (fig. S18) (*39*–*41*). Compared to the pristine SSO, the Sn 3d, Sb 3d, and Sb 3p XPS spectra of Ir-Sn PSC are all shifted to higher binding energy, signifying that the Sn and Sb elements have suffered from a partial oxidation process during the formation of Ir-Sn PSC (figs. S19 to S22) (*42*, *43*). These results suggest the presence of strong electronic interactions between Sb/Sn and Ir species during the synthesis of Ir-Sn PSC.

X-ray absorption near-edge structure (XANES) and extended x-ray absorption fine structure (EXAFS) were further carried out to probe the chemical states and local ligand fields of Ir-Sn PSC. As demonstrated in Fig. 2B, the intensity of the Ir L_3-edge XANES white line of Ir-Sn PSC is between those of Ir foil and the IrO_2 standard but lower than for Ir NPs, suggesting that the average valence state of Ir is in this sequence: Ir foil (Ir^0) < Ir-Sn PSC < Ir NPs < IrO_2 (Ir^{4+}) (*44*, *45*). This is well supported by the positive shift in the second derivative of the Ir L_3-edge XANES spectrum, illustrating the increased Ir 5d electron density in Ir-Sn PSC compared to Ir NPs (fig. S23) (*46*). The linear fitting results indicate that the *d*-band hole count of Ir-Sn PSC is 3.29, close to that of Ir foil (*3*) but lower than that of Ir NPs (3.96), indicating that Ir-Sn PSC has an almost metallic state, which suggests the formation of Ir-Sn PSC contributing to the reduction of the number of *d*-band holes in Ir (Fig. 2D, fig. S24, and table S2) (*47*, *48*). This is well in agreement with the linear combination fitting results of the Ir L_3-edge XANES spectra of Ir NPs and Ir-Sn PSC, in which about 80.9% of the Ir in Ir-Sn PSC is the metallic state, whereas only around 58.8% is in the

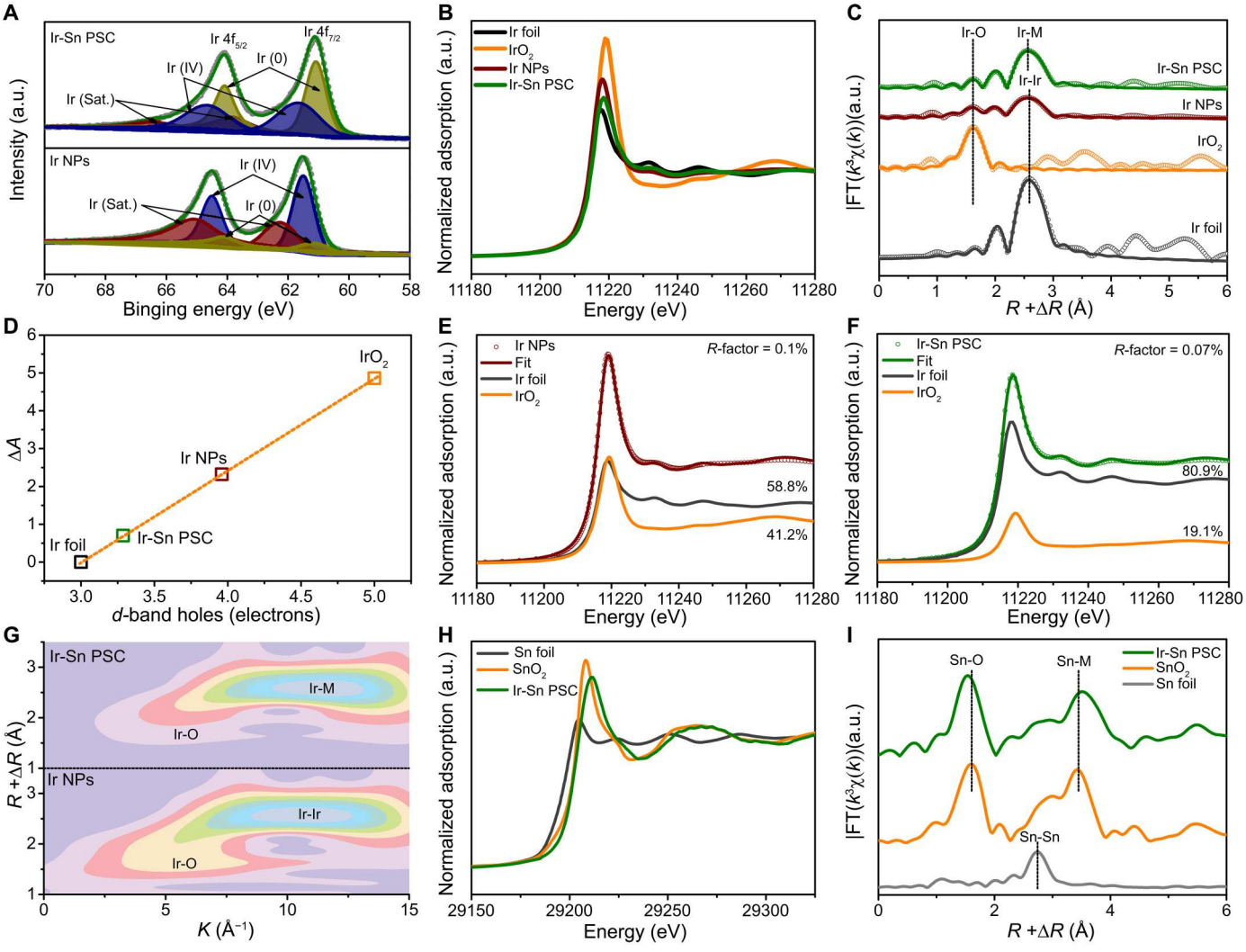

Fig. 2. Electronic structure of Ir-Sn PSC. (**A**) High-resolution Ir 4f XPS spectra of Ir NPs and Ir-Sn PSC. (**B**) Ir L_3-edge XANES spectra of Ir foil, IrO_2, Ir NPs, and Ir-Sn PSC. (**C**) The Ir L_3-edge EXAFS spectra (points) and curve fits (lines) for Ir foil, Ir NPs, IrO_2, and Ir-Sn PSC. The data are k^3-weighted and not phase-corrected. (**D**) White line peak area difference as a function of the formal *d*-band hole count. Ir L_3-edge XANES spectra fitting results for (**E**) Ir NPs and (**F**) Ir-Sn PSC. (**G**) WT-EXAFS contour maps of the Ir L_3-edge for Ir NPs and Ir-Sn PSC. (**H**) Sn K-edge XANES spectra of Sn foil, Ir-Sn PSC, and SnO_2. (**I**) The corresponding Sn K-edge EXAFS spectra (points) and curve fits (lines). The data are k^3-weighted and not phase-corrected. a.u., arbitrary units.

Ir NPs (Fig. 2, E and F; fig. S25; and table S3). The weakened Ir-O scattering in the wavelet transform (WT) of Ir L_3-edge EXAFS contour maps for Ir-Sn PSC also offers compelling evidence to support this conclusion (Fig. 2G and fig. S26). An inconspicuous peak at ~1.62 Å and another notable peak situated at ~2.5 Å are observed in the Ir L_3-edge FT-EXAFS spectra of Ir NPs and Ir-Sn PSC, which could be assigned to the contribution of Ir-O and Ir-M (M = Ir, Sn, and Sb) scattering, respectively (Fig. 2C) (*49*, *50*). The FT-EXAFS fitting results further reinforce the substantial role of the heterointerface in impeding the oxidation of Ir NPs with a lower coordination number of ~2.0 for the Ir-O path and a higher ligand number of ~8.6 for Ir-M scattering in Ir-Sn PSC than those of Ir NPs, which are ~3.1 and ~6.2 for the Ir-O and Ir-Ir path, respectively (fig. S27 and table S4). Moreover, the Sn K-edge XANES spectrum for Ir-Sn PSC shows that the absorption edge has a slightly positive shift toward higher energy compared to SnO_2, which implies the slight oxidation of Sn with a higher valence state than +4 in Ir-Sn PSC, in good agreement with the analysis results of XPS (Fig. 2H) (*42*, *51*). The Sn K-edge FT-EXAFS spectrum of Ir-Sn PSC exhibits a prominent peak at ~1.54 Å, derived from the contribution of the Sn-O path, and another peak at ~3.51 Å contributed by the Sn-M coordination, which is well supported by the WT-EXAFS analysis with the presence of Sn-O and Sn-M coordination in Ir-Sn PSC (Fig. 2I and figs. S28 and S29) (*51*, *52*). The negative shift of the Sn-O path in Ir-Sn PSC is probably caused by the reduced ionic radius of Sn due to oxidation, resulting in the contraction of the Sn-O bond length. Overall, the spectroscopic analyses collectively reveal possible charge transfer between Ir-Sn/Sb sites around the interface during the formation of Ir-Sn PSC, which triggers the strong electronic metal–support interactions (EMSI) and plays a vital role in impeding the overoxidation of Ir species.

Electrocatalytic performance

The polarization curves reveal that the catalytic activities can be boosted by increasing the mass loading of Ir, in which the required overpotentials for current densities of 10 and 100 mA cm^{-2} can be reduced from 225 and 324 mV (10.2% Ir-Sn PSC) to 200 and 299 mV (Ir-Sn PSC) and 193 and 264 mV (38.2% Ir-Sn PSC) (fig. S30). Similarly, we selected Ir-Sn PSC as the representative catalyst to systematically elucidate the extraordinary structure-activity dependence. The Ir-Sn PSC also delivered superior activity to those of the control catalysts, with the overpotentials of 35 and 172 mV smaller than for Ir NPs and commercial IrO_2 at 10 mA cm^{-2}, and this difference could reach 53 and 334 mV on increasing the current density to 40 mA cm^{-2} (Fig. 3, A and B, and table S5). The Ir-Sn PSC could exhibit an extremely high mass activity of 2.9 A mg_{Ir}^{-1} at an overpotential of 320 mV, which is more than one and two orders of magnitude higher than for Ir NPs and IrO_2, respectively (Fig. 3C and fig. S31). It should be mentioned that the mass activity could be further enhanced to 4.4 A mg_{Ir}^{-1} by reducing the Ir mass loading to 10.2 wt %. The acidic OER activity of Ir-Sn PSC is superior to those of most of the state-of-the-art catalysts reported in previous works, suggesting its unique structural superiority (table S6). Moreover, the lowest Tafel slope of Ir-Sn PSC (64.1 mV dec^{-1}) suggests rapid mass and charge transfer kinetics processes (Fig. 3D). The electrochemical impedance spectroscopy results (fig. S32) demonstrate that Ir-Sn PSC exhibits the lowest charge transfer resistance (~3 ohms), much smaller than that of Ir NPs (~7 ohms) and IrO_2 (~329 ohms), illustrating the substantially enhanced reaction kinetics. Also, the Ir-Sn PSC exhibits a high turnover frequency (TOF) of 1.06 s^{-1}, about 11 and 105 times higher than those of Ir NPs and IrO_2, respectively, illustrating the considerably enhanced intrinsic activity of Ir-Sn PSC (Fig. 3E). The electrochemical double-layer capacitance (C_{dl}) derived from the cyclic voltammetry (CV) curves suggest that the Ir-Sn PSC features much more exposed catalytically active sites (Fig. 3F and fig. S33). This could be attributed to the crucial role of SSO, which provides abundant surface sites to anchor and inhibit the Ir species to avoid aggregation.

Chronopotentiometry (CP) measurements indicated that the Ir-Sn PSC exhibits excellent durability without obvious decay after 180 hours of operation at the current density of 30 mA cm^{-2} in 0.5 M H_2SO_4, whereas the IrO_2 could only survive for several hours, demonstrating the high corrosion resistance of Ir-Sn PSC in an acidic and oxidative environment (fig. S34) (*53*, *54*). This is supported by the well-maintained crystal structure of Ir-Sn PSC after the stability test (fig. S35). Inspired by the substantial advances in both activity and durability, a water-splitting cell was assembled with Ir-Sn PSC and Pt/C as OER and Hydrogen Evolution Reaction (HER) catalysts, respectively. The Ir-Sn PSC||Pt/C cell exhibited both lower overpotential and higher cycling stability, with only 0.46 mV/hour decay at 20 mA cm^{-2} for 260 hours of operation, two orders of magnitude more than that of the IrO_2|| Pt/C cell (Fig. 3G and fig. S36).

Studies on the long-term stability

To explore why Ir-Sn PSC exhibits outstanding long-term durability during the acidic OER, we have carefully examined the crystal structure, morphology, and electronic structure of cycled Ir-Sn PSC catalysts. The XRD results indicate that the crystal structure of cycled Ir-Sn PSC is well-maintained even after 260 hours of operation at 20 mA cm^{-2} in 0.5 H_2SO_4, suggesting that Ir-Sn PSC features an outstanding corrosion-resistant ability to avoid structural decay due to the formation of Ir-Sn dual-atom site at the interface (Fig. 4A and fig. S37). HAADF-STEM and ABF-STEM images demonstrated that the morphology and heterointerfaces of cycled Ir-Sn PSC are well-preserved, and the observed characteristic lattice facets of Ir and SSO [e.g., Ir (111) and SSO (101)] further collectively highlight the structural superiority of Ir-Sn PSC. (Fig. 4B and figs. S38 and S39). The evolution of the electronic states and coordination environment of cycled Ir-Sn PSC was further deciphered by various spectroscopic characterizations. The positive shift of the Ir 4f, Sn 3d, and Sb 3d spectra of cycled Ir-Sn PSC suggests the slight oxidation of Ir, Sn, and Sb after the long-term stability test (fig. S40). The Ir L_3-edge XANES spectra indicated that the average oxidation state of Ir in cycled Ir-Sn PSC was higher than that of pristine Ir-Sn PSC but lower than that of IrO_2 (Fig. 4C). The calculated number of *d*-band holes of cycled Ir-Sn PSC is about 4.3, larger than for Ir-Sn PSC (3.29) but smaller than for IrO_2 (*5*), and this trend correlates well with the XANES fitting results, in which the metallic Ir^0 and oxidized Ir^{4+} are 35.6 and 64.4% of Ir content, respectively, manifesting that the metallic state is maintained, even after long-term cycling (Fig. 4D and figs. S41 and S42).

This is further evidenced by the enhanced intensity of the Ir-O path with higher coordination numbers (around 4.3) and the maintained Ir-M peak in the Ir L_3-edge FT-EXAFS spectrum of cycled Ir-Sn PSC when compared to that of the pristine one (Fig. 4E and fig. S43). Moreover, the WT results also confirm the presence of more

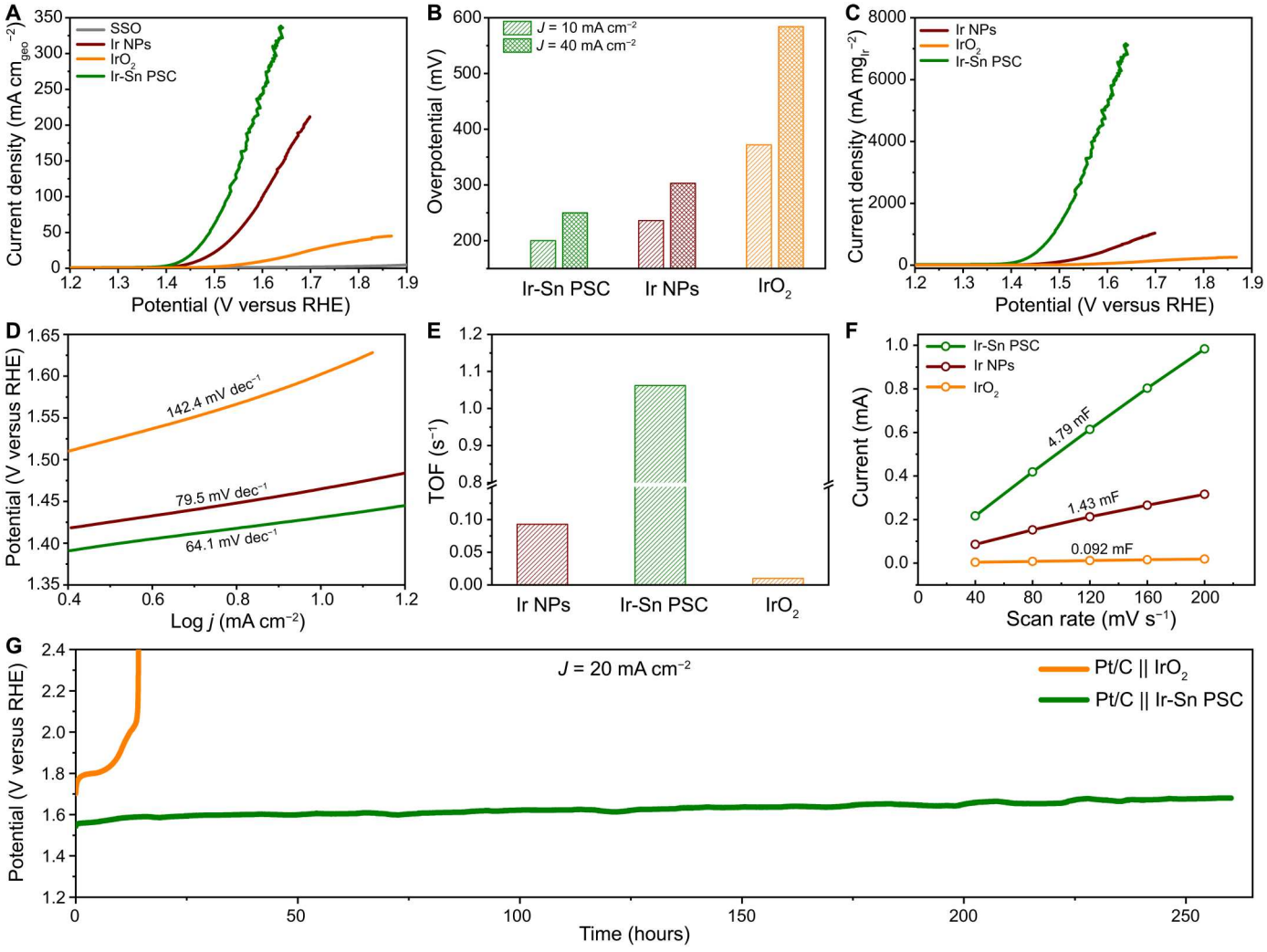

Fig. 3. OER performance of Ir-Sn PSC. (**A**) Polarization curves of SSO, Ir NPs, Ir-Sn PSC, and IrO_2. (**B**) The corresponding overpotential at the current densities of 10 and 40 mA cm^2. (**C**) Linear sweep voltammetry curves based on the mass activity of Ir. (**D**) Tafel slopes of Ir NPs, Ir-Sn PSC, and IrO_2. (**E**) TOFs based on the mass of Ir. (**F**) C_{dl} plots. (**G**) Long-term durability test for full cells for water splitting assembled with Pt/C and Ir-Sn PSC at the current density of 20 mA cm^2.

prominent Ir-O and retained Ir-M coordination in cycled Ir-Sn PSC compared to Ir-Sn PSC_OER and Ir-Sn PSC (Fig. 4F and fig. S44) The maintenance of the Ir-M scattering featured in the cycled Ir-Sn PSC suggests the retained metallic nature of Ir species in the Ir-Sn PSC, even after 260 hours of operation at 20 mA cm^{-2}. The metal dissolution was determined by inductively coupled plasma optical emission spectroscopy (ICP-OES), revealing that only approximately 12% of the Ir in Ir-Sn PSC was dissolved into the solution after 192 hours of operation (fig. S45). Moreover, it can be inferred that the electronic interaction between Ir and Sb also plays a vital role in enhancing the stability of the Ir-Sn PSC. The superior durability of Ir-Sn PSC might arise from the unique heterostructured architecture with the presence of Ir-Sn dual-atom site around the interface, offering abundant sites to anchor Ir species and inhibit their migration, aggregation, and dissolution during the OER process, as well as the triggered strong electronic interaction to suppress the overoxidation of Ir species via spontaneously delivering charge from to Ir to SSO in the Ir-Sn PSC.

Encouraged by both its superior activity and durability, we assembled a PEMWE using Ir-Sn PSC as the anode catalyst with a mass loading of 1 mg cm^{-2} (Fig. 4G). The polarization curve indicated that the Ir-Sn PSC can deliver a high current density of 1 and 2 A cm^{-2} with only 1.548 and 1.711 V, respectively, comparable to most reported PEMWE devices using state-of-the-art electrocatalysts (fig. S46 and table S7). Furthermore, the PEMWE assembled with Ir-Sn PSC also exhibited excellent durability with only 0.88 mV/hour decay rate at the current density of 1 A cm^{-2}, rendering it attractive as a potential acidic OER electrocatalyst for practical applications (Fig. 4H).

Operando spectroscopic characterizations during the OER process

To further unravel the underlying dynamic catalytic mechanisms of Ir-Sn PSC, we combined operando XAS and x-ray emission spectroscopy (XES) techniques to examine the evolution of the electronic structure of Ir and Sn during the OER process. With increasing the

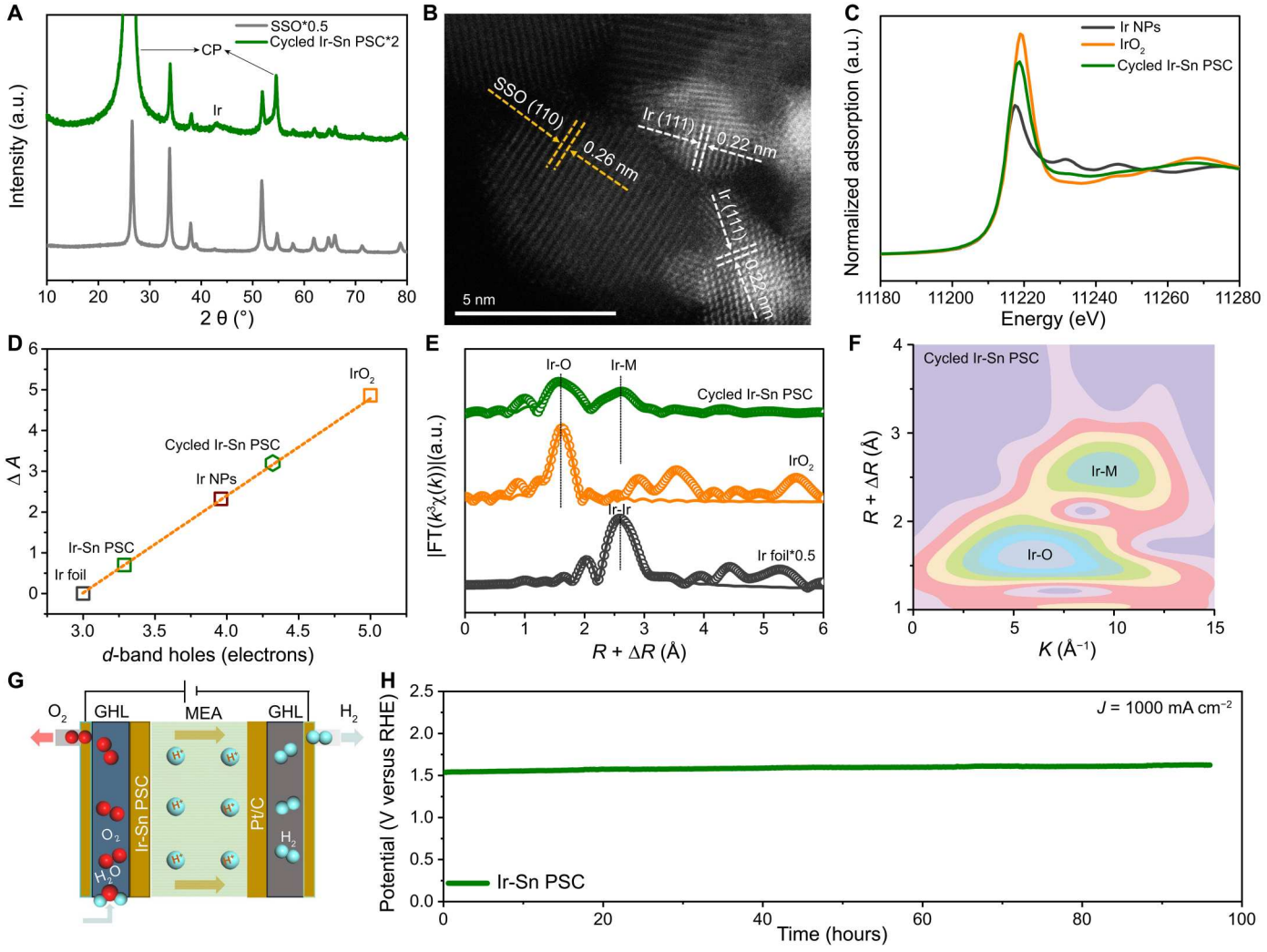

Fig. 4. Structural characterization of cycled Ir-Sn PSC. (**A**) XRD pattern. (**B**) HAADF-STEM image. (**C**) Ir L_3-edge XANES spectra of Ir foil, IrO_2, and cycled Ir-Sn PSC. (**D**) White line peak area difference as a function of the formal *d*-band hole count. (**E**) Ir L_3-edge EXAFS spectra (points) and curve fits (lines) for Ir foil, IrO_2, and cycled Ir-Sn PSC, shown in *R* space. (**F**) WT-EXAFS contour map of Ir L_3-edge for cycled Ir-Sn PSC. (**G**) Schematic illustration of PEMWE using Ir-Sn PSC as the anode catalyst. (**H**) CP test of PEMWE using Ir-Sn PSC operated at 1000 mA cm^{-2}.

applied voltage from the open circuit potential to 1.6 V, the white line intensity of the Ir L_3-edge XANES spectra of Ir-Sn PSC increased gradually, along with a slight positive shift to higher energy (Fig. 5A and fig. S47). This suggests the gradual enrichment of *d*-band holes and reduced 5d electron density of Ir species under potential-driven conditions, implying an increase in the oxidation state of Ir in Ir-Sn PSC (*55*). Meanwhile, the slight shift of the white line position and the increased intensity suggest the crucial role of the heterointerface in suppressing the over-oxidation of Ir species during the OER process, thereby substantially mitigating metal dissolution. Moreover, a peak located at ~1.64 Å, which can be attributed to Ir-O coordination, becomes pronounced at 1.6 V, manifesting the dynamic evolution of surface Ir species during the OER process (Fig. 5B) (*56*). Despite the oxidation of surface Ir species at high potential, the well-maintained intensity of Ir-M coordination evidences the metallic nature of Ir species in Ir-Sn PSC during the OER (fig. S48) (*57*). Moreover, this dynamic evolution process can be vividly illustrated by the gradual change of the Ir L_3-edge WT-EXAFS plots, where the Ir-O scattering becomes increasingly obvious and Ir-M scattering maintains well with improved potential bias (fig. S49). In addition, there is a slightly positive shift of the absorption edge for Sn K-edge XANES from the open circuit potential to 1.4 V, suggesting that the slight oxidation of Sn is probably related to the increased potential (Fig. 5C) (*58*, *59*). This indicates that strong electronic interaction exists between Ir and Sn sites, in which the SSO could act as an electron reservoir to provide the extra electrons to oxygen species for Ir species at higher potential, and in turn hinders the formation of soluble Ir^{6+}-containing species to prevent the overoxidation of Ir. Also, the WT and FT-EXAFS results further verify the well-kept Sn-O and Sn-M coordination in Ir-Sn PSC during the OER process (figs. S50 and S51). In addition, we conducted operando XES to examine the dynamic electronic evolution of Ir sites in Ir-Sn PSC (*60*, *61*). The characteristics L_{b1} feature with a peak at ~10,709 eV was observed for the Ir

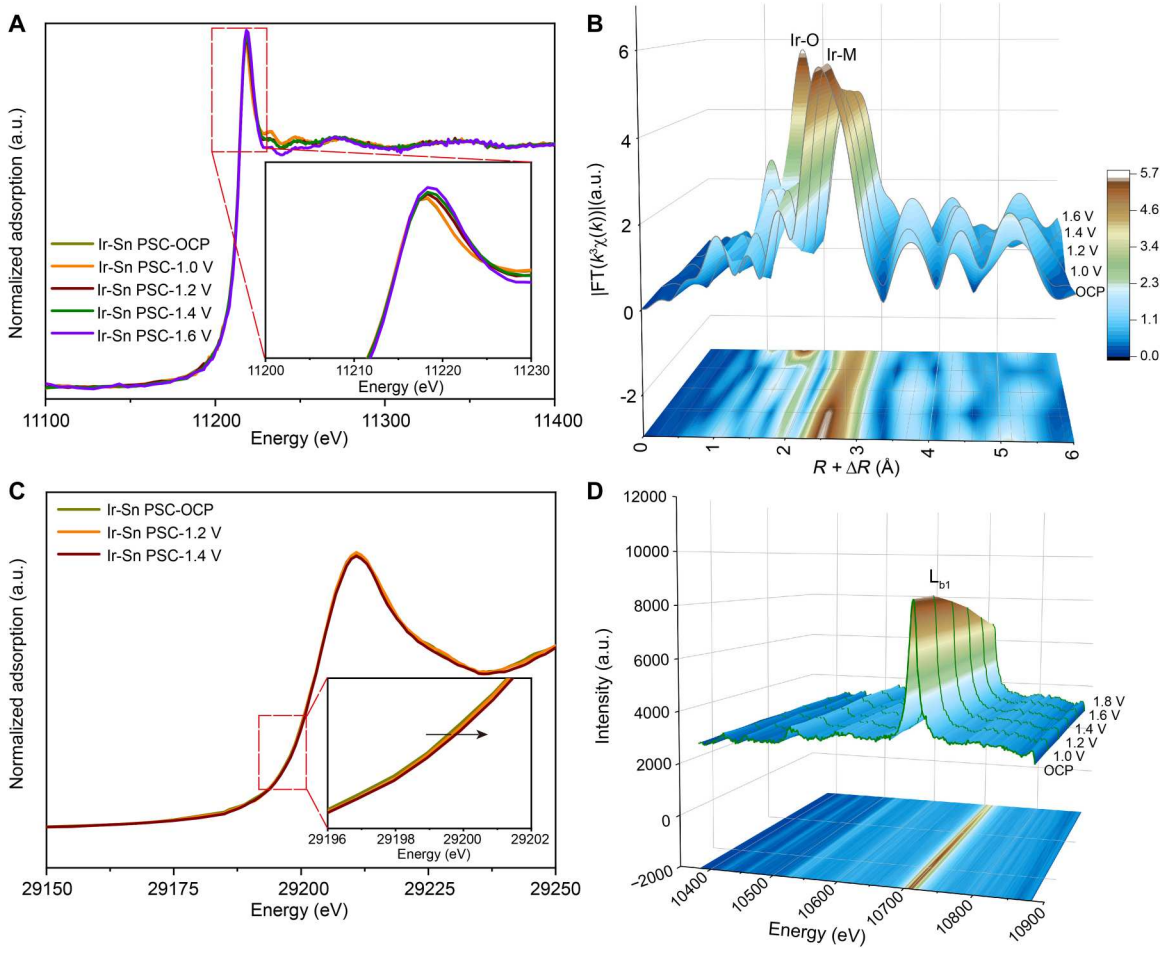

Fig. 5. Dynamic evolution of the electronic structure of Ir-Sn PSC during the OER process. (**A**) Operando XANES spectra of the Ir L_3-edge for Ir-Sn PSC at different voltages. The inset is the magnified image in the red rectangle area shown in (A). (**B**) The corresponding Ir L_3-edge EXAFS spectra, shown in *R* space. The data are k^3-weighted and not phase-corrected. (**C**) Operando Sn K-edge XANES spectra. Inset is an enlargement figure of the indicated range in (C). (**D**) Operando Ir L_{b1} XES spectra recorded on Ir-Sn PSC from open circuit potential to 1.8 V versus RHE.

foil, IrO_2, and Ir-Sn PSC sample, which can be assigned to the Ir $3d_{3/2}$ (L_2) to Ir $2p_{1/2}$ (M_4) dipole transition (fig. S52). The gradually positively shifted L_{b1} peak demonstrates an oxidation process of Ir species with increased potential which could be reasonable as more available d holes could cause poorer screening, resulting in a larger chemical shift, well consistent with the operando XAS results (Fig. 5D and fig. S53) (*62*).

We further examined the evolution of the crystal structure, morphology, and electronic properties of Ir-Sn PSC after several OER cycles (Ir-Sn PSC_OER) by ex situ XPS and XAS. The microscopic characterizations demonstrated that the crystal structure and the morphology were well-maintained (figs. S54 to S61). The maintenance of the metallic iridium phase can be discerned by carefully examining the atomic arrangement of Ir, which is in good agreement with the crystal structure of metallic Ir viewed from the [011] zone axis rather than that of the IrO_2 from the [001] direction (figs. S58 and S59). The lower Ir 4f binding energy and the maintained Ir^0 component of Ir-Sn PSC suggest its good oxidation resistance capability with only slight oxidation, which might be beneficial for enhancing long-term durability (fig. S62 and table S8). This is also supported by the retained Sn 3d, Sb 3d, and 2p XPS spectra in Ir-Sn PSC_OER (fig. S63). The linear combination fitting results for L_3-edge XANES spectra indicate that only ~7% metallic Ir is oxidized in Ir-Sn PSC_OER, which is consistent with the small increase in *d*-band holes to 3.4 (figs. S64 and S65). The emerging Ir-O path with higher coordination numbers (~2.3) in Ir-Sn PSC_OER than the pristine one and the maintained Ir-M scattering in the Ir L_3-edge FT and WT-EXAFS spectra jointly support the slight oxidation of surficial Ir species after OER cycling of Ir-Sn PSC (figs. S66 and S67). These results suggest that there is probably a dynamic equilibrium between surface Ir oxidation and reduction due to the unique heterostructured architecture of Ir-Sn PSC, which could greatly suppress the rapid oxidation of Ir metal.

Theoretical insights on the OER activity and stability

After thoroughly discussing the structure-performance relationship based on the results of experimental characterizations, it is imperative to provide detailed theoretical insights down to the electronic level. Four-electron OER pathways based on the adsorbate evolution mechanism on IrO_2 (110) and Ir-Sn PSC were studied by exploring and comparing the energetics of the corresponding adsorption

intermediates (fig. S68). As indicated in Fig. 6A, the potential-determining step of Ir-Sn PSC is the formation of *OOH derived from the attack of H_2O to O radical, which features a small energy barrier of 1.56 eV, much lower than that of IrO_2 (1.66 eV) (table S9). Also, Ir-Sn PSC shows a near-optimal ΔG_O-ΔG_{OH} (1.19 eV), very close to the theoretical value (1.23 eV) and low theoretical overpotential of only 0.33 V (fig. S69 and table S10), suggesting a higher OER activity, in good agreement with the experimental results (*40*).

Yet, how is this amazing performance of Ir-Sn PSC achieved? First of all, the EMSI of Ir-Sn PSC is essential for enhanced activity. As demonstrated by the charge density difference results, there is a large amount of electron exchange between the Ir species and the SSO substrate, in good accordance with the spectroscopic characterization results, indicating the existence of a strong EMSI in Ir-Sn PSC (Fig. 6B and fig. S70). In addition, the strong electronic interactions of Ir-Sn and Ir-Sb are also revealed by the crystal orbital Hamilton population (COHP), supported by the large overlapping between Ir and Sn/Sb orbitals in the range from −12 to 0 eV (Fig. 6C and fig. S71). The EMSI could accelerate the electron transfer and enhance the binding capability, helping to effectively inhibit the aggregation and impede the dissolution of Ir species from the host material during the OER process (*63*).

In addition, the proper EMSI could modify the electronic environment of the Ir species. The electrostatic potential and the

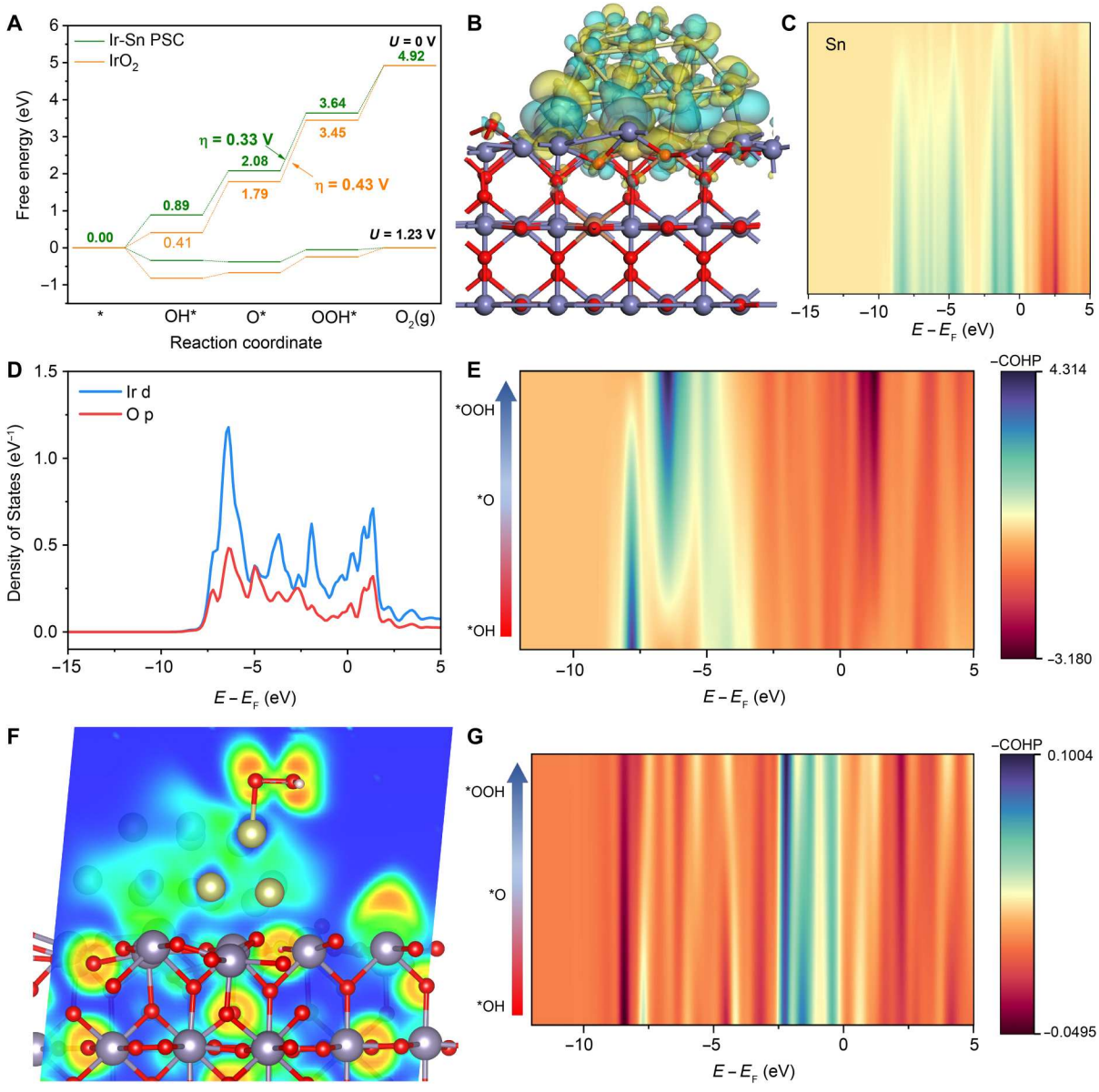

Fig. 6. Electronic properties of Ir-Sn PSC. (**A**) Gibbs free energy diagram of IrO_2 (110) and Ir-Sn PSC at U = 0 V and U = 1.23 V, where U is the potential under standard conditions versus RHE. (**B**) Charge density difference of Ir-Sn PSC. The cyan and yellow isosurfaces show electron density accumulation and depletion, respectively. (**C**) The COHP of the Ir atoms at different heights and Sn atoms on the surface of the Ir-Sn PSC. (**D**) DOS of Ir 5d orbital and the adsorbed O 2p orbital in Ir-Sn PSC-O*. (**E**) The COHP evolution of Ir-O after the adsorption of O*, OH*, and OOH*. (**F**) The ELF of the Ir-Sn PSC-OOH*. (**G**) The COHP evolution of Ir-Sn after the adsorption of O*, OH*, and OOH*.

electron localization function (ELF) analysis results indicated that there are synergistic effects on Ir atoms (Fig. 6F and figs. S72 and S73). In the acidic media, the water molecules often exist in the form of H_3O^+, which needs binding sites featuring nucleophilic and electrophilic properties simultaneously. The electrostatic potential analysis revealed that the Ir atoms exhibited middle-level properties of gain and loss of electrons, which is favorable for the enrichment of the reactant (i.e., H_3O^+) and the adsorption of O-end intermediates for further oxidation (fig. S72). Similarly, the ELF values of the active sites were lower than 0.4, meaning that the oxidation process of the reactant is not only restricted to a single Ir atom but also has to do with the neighboring Ir sites (fig. S73). As claimed above, the surrounding Ir atoms play the role of anchoring the H atom on H_3O^+, thereby enriching the reactant. Meanwhile, the highly discrete electron cloud distribution on Ir-Sn PSC contributes to accelerating the surface electron exchange-and-transfer capability. The EMSI accelerates the rate-determining step of *OOH formation, which is the key to the system. Analyses of the density of states (DOS) and COHP reveal the main aspects (figs. S74 to S76). When the DOS of the Ir site with the adsorption of O is put forward, the orbitals for adsorbed O and Ir anchoring sites are amazingly consistent from −8 to 3 eV (Fig. 6D). There is a large contribution of antibonding orbitals, however, as shown by the corresponding COHP (fig. S76). It can be concluded that, although there are a large number of electron transitions and strong interactions between O and Ir, the adsorption is relatively weak. From the Bader charge analysis, the adsorbed O atom has a charge of −0.72 e, so it is more likely oxygen radical. The O radical is very active, which accelerates the formation of *OOH in the following step (*32*). These results can also be supported by an experimental phenomenon. The bubbles on the catalysts are very small and arise beyond the surface, indicating that the O_2 may not exactly obey the desorption rule but rather the process of radical quenching. Therefore, the right combination between Ir and SSO achieves the proper EMSI, which realizes the formation of O radicals during the reaction and accelerates the oxygen evolution kinetics.

Upon further analysis of the process, intriguing coincidences come to light. As the COHP changes during the OER process (Fig. 6E), a new positive peak emerges at approximately −6 eV. This peak can be attributed to the strong electronic interaction between Ir and O, facilitating efficient electron transfer to the reactant. Simultaneously, there are also other new negative peaks located at −2.5 to 1.5 eV, which represent antibonds between Ir and O. These antibonds are mainly attributed to the π* interaction between Ir $5d_{z^2}$-O $2p_y$ and Ir $5d_{xz}$-O $2p_x$, located at ~1 eV above the Fermi level, which can be occupied during the OER process (over 1.23 V versus RHE) (fig. S75). It thus provides alternative orbitals for electron transfer from Ir sites, resulting in the formation of O radicals (fig. S77). Amazingly, the electronic interactions of Ir-Sn pair-site show similar changes at the same energy level during the OER process (Fig. 6G and fig. S78). This indicates that the electron lost from the O atom is quickly transferred to the substrate, accelerating the formation of an O radical and preventing the overoxidation of the Ir species.

DISCUSSION

In summary, we report an antioxidation strategy to boost anode corrosion resistance by triggering oxygen radicals via elaborately constructing heterostructured Ir-Sn PSC. The substantially enhanced catalytic performance of Ir-Sn PSC could be attributed to the formation of heterointerface with the Ir-Sn dual-atom site, which offers abundant interfaces, enabling substantially increased catalytically active sites and accelerated charge transfer kinetics. Moreover, the Ir-Sn PSC has a favorable electronic structure and coordination environment to realize near-optimal oxygen adsorption energetics and triggers oxygen radicals by the strong electronic interactions to suppress Ir overoxidation. This study not only provides a highly efficient and long-lived device-oriented electrocatalyst but also offers important insights into manipulating free radicals to realize antioxidation for anodic protection.

MATERIALS AND METHODS

Preparation of Ir-Sn PSC

Ir-Sn PSC was prepared by a facile wet chemical method. Specifically, 12 mg of antimony tin oxide (99.5%, Alfa Aesar) and 80 mg of P123 (Macklin) were added to 15 ml of ethylene glycol (99%, Sigma-Aldrich). The mixture was ultrasonicated for 30 min to obtain a homogeneous solution. Then, different contents (0.312, 0.832, and 1.873 ml) of 0.05 M $IrCl_4$ xH_2O (99%, Aladdin) were added into the homogeneous solution and ultrasonicated for another 30 min, respectively. The obtained solution was heated and stirred (1200 rpm/min) at 120°C for 3 hours in an oil bath. The suspension was washed with ethanol and deionized water and then centrifuged several times, followed by drying in a vacuum oven for 12 hours. The actual loaded Ir metal content was evaluated by ICP mass spectroscopy, which were 10.2, 23.2, and 38.3%, respectively. For comparison, the synthesis of pure Ir NPs was the same as for Ir-Sn PSC, only without adding the SSO support.

Material characterization

XRD was performed on a D/max-2550 x-ray diffractometer with a sweep rate of 5° min^{-1} from 10° to 80°. The morphology of the Ir-Sn PSC catalysts was characterized by TEM (JEM-2100F). The atomic arrangement of Ir-Sn PSC was examined by HAADF-STEM and ABF-STEM (JEOL ARM300F). The mass loading of Ir and leached Ir, Sn, and Sb contents were determined by ICP-OES (Optima-7000DV). The valence states of all the elements (Ir, Sn, Sb, and O) were assessed by XPS using an ESCALAB Xi^+Analyser (Thermo Fisher Scientific) installed in a high-vacuum chamber (below 10^{-9} mbar), and x-ray excitation was provided by Al Kα radiation at the high voltage of 15 kV. The XAS spectra were collected at Beamline BL14W1 and the BL11B station at the Shanghai Synchrotron Radiation Facility (SSRF) and the 1W1B station at the Beijing Synchrotron Radiation Facility (BSRF). The obtained XANES and EXAFS data were analyzed using Athena and Artemis software, respectively (*64*).

Operando XAFS measurements

Operando XAFS measurements of Ir L_3-edge spectra were recorded at the BL14W1 station in the SSRF, China. The storage ring of SSRF is operated at 3.5 GeV with a multibunch current up to 300 mA. The operando XAFS measurements were carried out using a homemade cell in 0.5 M H_2SO_4 solution. The Ir L_3-edge XAFS spectra were collected in transmission/fluorescence mode. The Ir-Sn PSC ink was coated on carbon paper (1 cm by 2 cm) with a mass loading of

0.5 mg cm^{-2}. The data were recorded at different voltages, including the onset potential, 1.0, 1.2, 1.4, and 1.6 V versus RHE. The absorption edge energy (E_0) of Ir L_3-edge spectra was calibrated using a standard sample of Ir foil. The Sn K-edge XAFS spectra were recorded at the BL11B station in the SSRF. The energy calibration of the Sn K-edge XAFS spectra was based on the standard sample of Sn foil.

Operando XES measurements

The operando XES spectra were collected at the beamline of 4W1B station in the BSRF, China. The storage ring runs 2.5-GeV electrons with a current of 250 mA. The operando XES measurements were carried out by a homemade cell in a 0.5 M H_2SO_4 solution. The Ir-Sn PSC ink was coated on carbon paper (1 cm by 2 cm) with a mass loading of 0.5 mg cm^{-2}. The data were recorded at different voltages including onset potential, 1.0, 1.2, 1.4, 1.6, and 1.8 V versus RHE. For the L_{b1} line of iridium element, Si (555) crystal was used. Also, Ir foil and IrO_2 were used as the reference samples for Ir^0 and Ir^{4+} valence states, respectively.

Electrochemical measurements

The catalyst ink was prepared by dispersing a mixture of the sample (4 mg) with VulcanXC-72 carbon (2 mg) into 1 ml of mixed solution (5% Nafion solution/deionized water/isopropanol = 4:96:25 by volume). Then, 10 μl of catalyst ink was dropped on glassy carbon and dried in ambient air. The OER performance was investigated with three-electrode systems (CHI 760) at a rotation speed of 1600 rpm in 0.5 M H_2SO_4 solution. Hg/Hg_2SO_4 was used as the reference electrode, and Pt mesh was used as the counter electrode, respectively. Linear sweep voltammetry was conducted at a scanning rate of 10 mV s^{-1}. The stability testing was performed with CP measurements at 30 mA cm^{-2} for 180 hours. Electrochemical impedance spectroscopy was carried out in the frequency range of 100 kHz to 0.1 Hz. All the potentials were *iR*-corrected by the resistance of the electrolyte unless explicitly stated.

The TOF values for all catalysts were evaluated by the following equation

$$\mathrm{TOF} = \frac{I}{4nF} \tag{1}$$

where I is the current (A) at an overpotential of 300 mV, F is the Faraday constant (96,485 C mol^{-1}), and n represents the number of moles of Ir in the Ir NPs, IrO_2, and Ir-Sn PSC.

The double-layer capacitance (C_{dl}) of all the catalysts was determined by conducting CV at different scanning rates. CV curves were recorded at different scanning rates from 40 to 200 mV s^{-1} in the voltage range of 1.166 to 1.266 V versus RHE. The C_{dl} was evaluated by the following equation

$$C_{dl} = \frac{|j_a| + |j_c|}{2\nu} \tag{2}$$

where j_a and j_b (mA cm^{-2}) are the anodic and cathodic current densities, respectively. ν is the scan rate (mV s^{-1}).

For the overall water-splitting performance assessment, catalyst ink (250 μl) was dropped on carbon paper (with mass loading of the catalyst 1 mg cm^{-2}) and dried at room temperature. Ir-Sn PSC and commercial Pt/C catalysts were applied as the anode (OER) and cathode (HER) catalysts for the assembly of the water-splitting device, and the cell was marked as Ir-Sn PSC||Pt/C. For comparison, an IrO_2||Pt/C cell using commercial IrO_2 and Pt/C as the anode and cathode catalyst, respectively, was assembled. The durability of the Ir-Sn PSC||Pt/C cell was recorded by CP measurements at a current density of 20 mA cm^{-2} for 260 hours. The potentials were without *iR* correction for the overall water-splitting test.

Electrochemical measurements in PEM water electrolyzer

A membrane electrode assembly was constructed using a treated N117 membrane. The obtained Ir-Sn PSC and commercial Pt/C (20 wt % Pt) were used as the anode and cathode catalysts for the PEMWE, respectively. The Pt/C and Ir-Sn PSC were deposited onto carbon paper and were used as the HER and OER catalysts, respectively. The surface area of the MEA was 2 cm by 2 cm (4 cm^2). The PEM electrolyzer was operated in H_2O under 80°C. The polarization curves of the PEMWE were recorded from the current density of 0.01 to 2.0 A cm^{-2}. The CP measurements were conducted at the current density of 1.0 A cm^{-2} to assess the long-term durability of PEMWE using an Ir-Sn PSC catalyst.

Theoretical calculations

All the DFT calculations were performed by using the Vienna Ab initio Simulation Program (*65*, *66*). The generalized gradient approximation in the Perdew-Burke-Ernzerhof form and cutoff energy of 500 eV for the plane-wave basis set were adopted (*67*). A 2 by 2 by 1 Monkhorst-Pack grid was used for sampling the Brillouin zones for structure optimization (*68*). The ion-electron interactions were described by the projector-augmented wave method (*69*). The convergence criteria of structure optimization were chosen with the maximum force on each atom less than 0.01 eV/Å, with an energy change of less than 1×10^{-5} eV. The DFT-D3 semiempirical correction was described via the Grimme's scheme method (*70*). To guarantee relaxations, a 15-Å vacuum space in the z axis was introduced. The calculation model was fully optimized before the electron properties and energy calculations.

The elementary steps are considered according to the following scheme.

$$2H_2O + * \rightarrow OH^* + H_2O + H^+ \tag{3}$$

$$OH^* + H_2O \rightarrow O^* + H_2O + e- + H^+ \tag{4}$$

$$O^* + H_2O \rightarrow OOH^* + e- + H^+ \tag{5}$$

$$OOH^* \rightarrow O_2 + *e- + H^+ \tag{6}$$

The Gibbs free energy of the elementary steps is calculated as

$$\Delta G_1 = \Delta G_{OH} - eU \tag{7}$$

$$\Delta G_2 = \Delta G_O - \Delta G_{OH} - eU \tag{8}$$

$$\Delta G_2 = \Delta G_{OOH} - \Delta G_O - eU \tag{9}$$

$$\Delta G_4 = 4.92\ \mathrm{eV} - \Delta G_{OOH} - eU \tag{10}$$

where U is the potential recorded under standard conditions (versus

RHE). The * is the adsorption site, and OH*, O*, and OOH* represent the OER reaction intermediates.

The Gibbs free energy difference was calculated based on $\Delta G = \Delta E + \Delta ZPE - T\Delta S$, and the energy differences ΔE are evaluated according to the energy of H_2O and H_2 (at $U = 0$ and pH = 0) as

$$\Delta E_{OH} = E(OH^*) - E(*) - [E(H_2O) - 0.5E(H_2)] \quad (11)$$

$$\Delta E_{O} = E(O^*) - E(*) - [E(H_2O) - E(H_2)] \quad (12)$$

$$\Delta E_{OOH} = E(OOH^*) - E(*) - [2E(H_2O) - 1.5E(H_2)] \quad (13)$$

The theoretical overpotential can be determined by the following equation

$$\eta = \max[\Delta G_1, \Delta G_2, \Delta G_3, \Delta G_4]/e - 1.23[V] \quad (14)$$

Supplementary Materials

This PDF file includes:

Figs. S1 to S78
Tables S1 to S10
References

REFERENCES AND NOTES

1. H. N. Nong, L. J. Falling, A. Bergmann, M. Klingenhof, H. P. Tran, C. Spori, R. Mom, J. Timoshenko, G. Zichittella, A. Knop-Gericke, S. Piccinin, J. Perez-Ramirez, B. R. Cuenya, R. Schlogl, P. Strasser, D. Teschner, T. E. Jones, Key role of chemistry versus bias in electrocatalytic oxygen evolution. *Nature* **587**, 408–413 (2020).
2. J. Hwang, R. R. Rao, L. Giordano, Y. Katayama, Y. Yu, Y. Shao-Horn, Perovskites in catalysis and electrocatalysis. *Science* **358**, 751–756 (2017).
3. J. Huang, H. Sheng, R. D. Ross, J. Han, X. Wang, B. Song, S. Jin, Modifying redox properties and local bonding of Co_3O_4 by CeO_2 enhances oxygen evolution catalysis in acid. *Nat. Commun.* **12**, 3036 (2021).
4. Y. Chen, H. Li, J. Wang, Y. Du, S. Xi, Y. Sun, M. Sherburne, J. W. Ager III, A. C. Fisher, Z. J. Xu, Exceptionally active iridium evolved from a pseudo-cubic perovskite for oxygen evolution in acid. *Nat. Commun.* **10**, 572 (2019).
5. L. C. Seitz, C. F. Dickens, K. Nishio, Y. Hikita, J. Montoya, A. Doyle, C. Kirk, A. Vojvodic, H. Y. Hwang, J. K. Norskov, T. F. Jaramillo, A highly active and stable $IrO_x/SrIrO_3$ catalyst for the oxygen evolution reaction. *Science* **353**, 1011–1014 (2016).
6. X. Zheng, J. Yang, P. Li, Z. Jiang, P. Zhu, Q. Wang, J. Wu, E. Zhang, W. Sun, S. Dou, D. Wang, Y. Li, Dual-atom support boosts nickel-catalyzed urea Electrooxidation. *Angew. Chem. Int. Ed.* **62**, e202217449 (2023).
7. J. Kibsgaard, I. Chorkendorff, Considerations for the scaling-up of water splitting catalysts. *Nat. Energy* **4**, 430–433 (2019).
8. D. G. Li, E. J. Park, W. L. Zhu, Q. R. Shi, Y. Zhou, H. Y. Tian, Y. H. Lin, A. Serov, B. Zulevi, E. D. Baca, C. Fujimoto, H. T. Chung, Y. S. Kim, Highly quaternized polystyrene ionomers for high performance anion exchange membrane water electrolysers. *Nat. Energy* **5**, 378–385 (2020).
9. C. Lin, J.-L. Li, X. Li, S. Yang, W. Luo, Y. Zhang, S.-H. Kim, D.-H. Kim, S. S. Shinde, Y.-F. Li, Z.-P. Liu, Z. Jiang, J.-H. Lee, In-situ reconstructed Ru atom array on α-MnO_2 with enhanced performance for acidic water oxidation. *Nat. Catal.* **4**, 1012–1023 (2021).
10. S. Pan, H. Li, D. Liu, R. Huang, X. Pan, D. Ren, J. Li, M. Shakouri, Q. Zhang, M. Wang, C. Wei, L. Mai, B. Zhang, Y. Zhao, Z. Wang, M. Graetzel, X. Zhang, Efficient and stable noble-metal-free catalyst for acidic water oxidation. *Nat. Commun.* **13**, 2294 (2022).
11. X. B. Zheng, B. B. Li, Q. S. Wang, D. S. Wang, Y. D. Li, Emerging low-nuclearity supported metal catalysts with atomic level precision for efficient heterogeneous catalysis. *Nano Res.* **15**, 7806–7839 (2022).
12. J. T. Mefford, A. R. Akbashev, M. Kang, C. L. Bentley, W. E. Gent, H. D. Deng, D. H. Alsem, Y. S. Yu, N. J. Salmon, D. A. Shapiro, P. R. Unwin, W. C. Chueh, Correlative operando microscopy of oxygen evolution electrocatalysts. *Nature* **593**, 67–73 (2021).
13. B. Zhang, X. Zheng, O. Voznyy, R. Comin, M. Bajdich, M. Garcia-Melchor, L. Han, J. Xu, M. Liu, L. Zheng, F. P. Garcia de Arquer, C. T. Dinh, F. Fan, M. Yuan, E. Yassitepe, N. Chen, T. Regier, P. Liu, Y. Li, P. De Luna, A. Janmohamed, H. L. Xin, H. Yang, A. Vojvodic, E. H. Sargent, Homogeneously dispersed multimetal oxygen-evolving catalysts. *Science* **352**, 333–337 (2016).
14. N. Danilovic, R. Subbaraman, K. C. Chang, S. H. Chang, Y. Kang, J. Snyder, A. P. Paulikas, D. Strmcnik, Y. T. Kim, D. Myers, V. R. Stamenkovic, N. M. Markovic, Using surface segregation to design stable Ru-Ir oxides for the oxygen evolution reaction in acidic environments. *Angew. Chem. Int. Ed.* **53**, 14016–14021 (2014).
15. X. Zheng, J. Yang, Z. Xu, Q. Wang, J. Wu, E. Zhang, S. Dou, W. Sun, D. Wang, Y. Li, Ru-Co pair sites catalyst boosts the energetics for the oxygen evolution reaction. *Angew. Chem. Int. Ed.* **61**, e202205946 (2022).
16. S. Li, B. Chen, Y. Wang, M. Y. Ye, P. A. van Aken, C. Cheng, A. Thomas, Oxygen-evolving catalytic atoms on metal carbides. *Nat. Mater.* **20**, 1240–1247 (2021).
17. Y. Lin, Z. Tian, L. Zhang, J. Ma, Z. Jiang, B. J. Deibert, R. Ge, L. Chen, Chromium-ruthenium oxide solid solution electrocatalyst for highly efficient oxygen evolution reaction in acidic media. *Nat. Commun.* **10**, 162 (2019).
18. A. Li, H. Ooka, N. Bonnet, T. Hayashi, Y. Sun, Q. Jiang, C. Li, H. Han, R. Nakamura, Stable potential windows for long-term electrocatalysis by manganese oxides under acidic conditions. *Angew. Chem. Int. Ed.* **58**, 5054–5058 (2019).
19. O. Kasian, J. P. Grote, S. Geiger, S. Cherevko, K. J. J. Mayrhofer, The common intermediates of oxygen evolution and dissolution reactions during water electrolysis on iridium. *Angew. Chem. Int. Ed.* **57**, 2488–2491 (2018).
20. Y.-R. Zheng, J. Vernieres, Z. Wang, K. Zhang, D. Hochfilzer, K. Krempl, T.-W. Liao, F. Presel, T. Altantzis, J. Fatermans, S. B. Scott, N. M. Secher, C. Moon, P. Liu, S. Bals, S. Van Aert, A. Cao, M. Anand, J. K. Nørskov, J. Kibsgaard, I. Chorkendorff, Monitoring oxygen production on mass-selected iridium–tantalum oxide electrocatalysts. *Nat. Energy* **7**, 55–64 (2022).
21. A. L. Li, S. Kong, C. X. Guo, H. Ooka, K. Adachi, D. Hashizume, Q. K. Jiang, H. X. Han, J. P. Xiao, R. Nakamura, Enhancing the stability of cobalt spinel oxide towards sustainable oxygen evolution in acid. *Nat. Catal.* **5**, 109–118 (2022).
22. X. Liu, S. Xi, H. Kim, A. Kumar, J. Lee, J. Wang, N. Q. Tran, T. Yang, X. Shao, M. Liang, M. G. Kim, H. Lee, Restructuring highly electron-deficient metal-metal oxides for boosting stability in acidic oxygen evolution reaction. *Nat. Commun.* **12**, 5676 (2021).
23. Y. Yao, S. Hu, W. Chen, Z.-Q. Huang, W. Wei, T. Yao, R. Liu, K. Zang, X. Wang, G. Wu, W. Yuan, T. Yuan, B. Zhu, W. Liu, Z. Li, D. He, Z. Xue, Y. Wang, X. Zheng, J. Dong, C.-R. Chang, Y. Chen, X. Hong, J. Luo, S. Wei, W.-X. Li, P. Strasser, Y. Wu, Y. Li, Engineering the electronic structure of single atom Ru sites via compressive strain boosts acidic water oxidation electrocatalysis. *Nat. Catal.* **2**, 304–313 (2019).
24. X. Liang, L. Shi, Y. Liu, H. Chen, R. Si, W. Yan, Q. Zhang, G. D. Li, L. Yang, X. Zou, Activating inert, nonprecious perovskites with iridium dopants for efficient oxygen evolution reaction under acidic conditions. *Angew. Chem. Int. Ed.* **58**, 7631–7635 (2019).
25. G. T. K. K. Gunasooriya, J. K. Nørskov, Analysis of acid-stable and active oxides for the oxygen evolution reaction. *ACS Energy Lett.* **5**, 3778–3787 (2020).
26. Z. Wang, Y.-R. Zheng, I. Chorkendorff, J. K. Nørskov, Acid-stable oxides for oxygen electrocatalysis. *ACS Energy Lett.* **5**, 2905–2908 (2020).
27. H. S. Oh, H. N. Nong, T. Reier, A. Bergmann, M. Gliech, J. Ferreira de Araujo, E. Willinger, R. Schlogl, D. Teschner, P. Strasser, Electrochemical catalyst-support effects and their stabilizing role for IrO_x nanoparticle catalysts during the oxygen evolution reaction. *J. Am. Chem. Soc.* **138**, 12552–12563 (2016).
28. H. N. Nong, H. S. Oh, T. Reier, E. Willinger, M. G. Willinger, V. Petkov, D. Teschner, P. Strasser, Oxide-supported IrNiOxCore–Shell particles as efficient, cost-effective, and stable catalysts for electrochemical water splitting. *Angew. Chem. Int. Ed.* **54**, 2975–2979 (2015).
29. H. S. Oh, H. N. Nong, T. Reier, M. Gliech, P. Strasser, Oxide-supported Ir nanodendrites with high activity and durability for the oxygen evolution reaction in acid PEM water electrolyzers. *Chem. Sci.* **6**, 3321–3328 (2015).
30. D. Böhm, M. Beetz, M. Schuster, K. Peters, A. G. Hufnagel, M. Döblinger, B. Böller, T. Bein, D. Fattakhova-Rohlfing, Efficient OER catalyst with low Ir volume density obtained by homogeneous deposition of iridium oxide nanoparticles on macroporous antimony-doped Tin oxide support. *Adv. Funct. Mater.* **30**, 1906670 (2019).
31. R. Z. Li, D. S. Wang, Understanding the structure-performance relationship of active sites at atomic scale. *Nano Res.* **15**, 6888–6923 (2022).
32. C. Ling, L. Q. Zhou, H. F. Jia, First-principles study of crystalline $CoWO_4$ as oxygen evolution reaction catalyst. *RSC Adv.* **4**, 24692–24697 (2014).
33. A. Grimaud, A. Demortière, M. Saubanère, W. Dachraoui, M. Duchamp, M.-L. Doublet, J.-M. Tarascon, Activation of surface oxygen sites on an iridium-based model catalyst for the oxygen evolution reaction. *Nat. Energy* **2**, 16189 (2017).
34. F. T. Haase, A. Bergmann, T. E. Jones, J. Timoshenko, A. Herzog, H. S. Jeon, C. Rettenmaier, B. R. Cuenya, Size effects and active state formation of cobalt oxide nanoparticles during the oxygen evolution reaction. *Nat. Energy* **7**, 765–773 (2022).
35. A. Hartig-Weiss, M. Miller, H. Beyer, A. Schmitt, A. Siebel, A. T. S. Freiberg, H. A. Gasteiger, H. A. El-Sayed, Iridium oxide catalyst supported on antimony-doped Tin oxide for high

oxygen evolution reaction activity in acidic media. *ACS Appl. Nano Mater.* **3**, 2185–2196 (2020).
36. G. Zhao, P. Li, N. Cheng, S. X. Dou, W. Sun, An Ir/Ni(OH)$_2$ heterostructured electrocatalyst for the oxygen evolution reaction: Breaking the scaling relation, stabilizing iridium(V), and beyond. *Adv. Mater.* **32**, e2000872 (2020).
37. H. Wang, Z. N. Chen, D. Wu, M. Cao, F. Sun, H. Zhang, H. You, W. Zhuang, R. Cao, Significantly enhanced overall water splitting performance by partial oxidation of Ir through Au modification in core-shell alloy structure. *J. Am. Chem. Soc.* **143**, 4639–4645 (2021).
38. R. Li, H. Wang, F. Hu, K. C. Chan, X. Liu, Z. Lu, J. Wang, Z. Li, L. Zeng, Y. Li, X. Wu, Y. Xiong, IrW nanochannel support enabling ultrastable electrocatalytic oxygen evolution at 2 A cm^{-2} in acidic media. *Nat. Commun.* **12**, 3540 (2021).
39. L. Zu, X. Qian, S. Zhao, Q. Liang, Y. E. Chen, M. Liu, B. J. Su, K. H. Wu, L. Qu, L. Duan, H. Zhan, J. Y. Zhang, C. Li, W. Li, J. Y. Juang, J. Zhu, D. Li, A. Yu, D. Zhao, Self-assembly of Ir-based nanosheets with ordered interlayer space for enhanced electrocatalytic water oxidation. *J. Am. Chem. Soc.* **144**, 2208–2217 (2022).
40. S. Hao, H. Sheng, M. Liu, J. Huang, G. Zheng, F. Zhang, X. Liu, Z. Su, J. Hu, Y. Qian, L. Zhou, Y. He, B. Song, L. Lei, X. Zhang, S. Jin, Torsion strained iridium oxide for efficient acidic water oxidation in proton exchange membrane electrolyzers. *Nat. Nanotechnol.* **16**, 1371–1377 (2021).
41. F. Zhao, B. Wen, W. Niu, Z. Chen, C. Yan, A. Selloni, C. G. Tully, X. Yang, B. E. Koel, Increasing iridium oxide activity for the oxygen evolution reaction with hafnium modification. *J. Am. Chem. Soc.* **143**, 15616–15623 (2021).
42. F. Luo, A. Roy, L. Silvioli, D. A. Cullen, A. Zitolo, M. T. Sougrati, I. C. Oguz, T. Mineva, D. Teschner, S. Wagner, J. Wen, F. Dionigi, U. I. Kramm, J. Rossmeisl, F. Jaouen, P. Strasser, P-block single-metal-site tin/nitrogen-doped carbon fuel cell cathode catalyst for oxygen reduction reaction. *Nat. Mater.* **19**, 1215–1223 (2020).
43. Z. Jiang, T. Wang, J. Pei, H. Shang, D. Zhou, H. Li, J. Dong, Y. Wang, R. Cao, Z. Zhuang, W. Chen, D. Wang, J. Zhang, Y. Li, Discovery of main group single Sb–N4active sites for CO_2 electroreduction to formate with high efficiency. *Energ. Environ. Sci.* **13**, 2856–2863 (2020).
44. Z. L. Fan, Y. J. Ji, Q. Shao, S. Z. Geng, W. X. Zhu, Y. Liu, F. Liao, Z. W. Hu, Y. C. Chang, C. W. Pao, Y. Y. Li, Z. H. Kang, M. W. Shao, Extraordinary acidic oxygen evolution on new phase 3R-iridium oxide. *Joule* **5**, 3221–3234 (2021).
45. Q. Dang, H. Lin, Z. Fan, L. Ma, Q. Shao, Y. Ji, F. Zheng, S. Geng, S. Z. Yang, N. Kong, W. Zhu, Y. Li, F. Liao, X. Huang, M. Shao, Iridium metallene oxide for acidic oxygen evolution catalysis. *Nat. Commun.* **12**, 6007 (2021).
46. Z. Shi, Y. Wang, J. Li, X. Wang, Y. Wang, Y. Li, W. Xu, Z. Jiang, C. Liu, W. Xing, J. Ge, Confined Ir single sites with triggered lattice oxygen redox: Toward boosted and sustained water oxidation catalysis. *Joule* **5**, 2164–2176 (2021).
47. W. H. Lee, Y. J. Ko, J. H. Kim, C. H. Choi, K. H. Chae, H. Kim, Y. J. Hwang, B. K. Min, P. Strasser, H. S. Oh, High crystallinity design of Ir-based catalysts drives catalytic reversibility for water electrolysis and fuel cells. *Nat. Commun.* **12**, 4271 (2021).
48. H. N. Nong, T. Reier, H.-S. Oh, M. Gliech, P. Paciok, T. H. T. Vu, D. Teschner, M. Heggen, V. Petkov, R. Schlögl, T. Jones, P. Strasser, A unique oxygen ligand environment facilitates water oxidation in hole-doped IrNiOx core–shell electrocatalysts. *Nat. Catal.* **1**, 841–851 (2018).
49. J. Shan, C. Guo, Y. Zhu, S. Chen, L. Song, M. Jaroniec, Y. Zheng, S.-Z. Qiao, Charge-redistribution-enhanced nanocrystalline Ru@IrOx electrocatalysts for oxygen evolution in acidic media. *Chem* **5**, 445–459 (2019).
50. J. Yin, J. Jin, M. Lu, B. Huang, H. Zhang, Y. Peng, P. Xi, C. H. Yan, Iridium single atoms coupling with oxygen vacancies boosts oxygen evolution reaction in acid media. *J. Am. Chem. Soc.* **142**, 18378–18386 (2020).
51. Q. Shi, Y. Ji, W. Chen, Y. Zhu, J. Li, H. Liu, Z. Li, S. Tian, L. Wang, Z. Zhong, L. Wang, J. Ma, Y. Li, F. Su, Single-atom Sn-Zn pairs in CuO catalyst promote dimethyldichlorosilane synthesis. *Natl. Sci. Rev.* **7**, 600–608 (2020).
52. A. Dutta, A. Kuzume, V. Kaliginedi, M. Rahaman, I. Sinev, M. Ahmadi, B. Roldán Cuenya, S. Vesztergom, P. Broekmann, Probing the chemical state of tin oxide NP catalysts during CO_2 electroreduction: A complementary operando approach. *Nano Energy* **53**, 828–840 (2018).
53. N. Li, L. Cai, C. Wang, Y. Lin, J. Huang, H. Sheng, H. Pan, W. Zhang, Q. Ji, H. Duan, W. Hu, W. Zhang, F. Hu, H. Tan, Z. Sun, B. Song, S. Jin, W. Yan, Identification of the active-layer structures for acidic oxygen evolution from 9R-BaIrO$_3$ electrocatalyst with enhanced iridium mass activity. *J. Am. Chem. Soc.* **143**, 18001–18009 (2021).
54. J. Chen, P. Cui, G. Zhao, K. Rui, M. Lao, Y. Chen, X. Zheng, Y. Jiang, H. Pan, S. X. Dou, W. Sun, Low-coordinate iridium oxide confined on graphitic carbon nitride for highly efficient oxygen evolution. *Angew. Chem. Int. Ed.* **58**, 12540–12544 (2019).
55. J. J. Velasco-Velez, E. A. Carbonio, C. H. Chuang, C. J. Hsu, J. F. Lee, R. Arrigo, M. Havecker, R. Wang, M. Plodinec, F. R. Wang, A. Centeno, A. Zurutuza, L. J. Falling, R. V. Mom, S. Hofmann, R. Schlogl, A. Knop-Gericke, T. E. Jones, Surface electron-hole rich species active in the electrocatalytic water oxidation. *J. Am. Chem. Soc.* **143**, 12524–12534 (2021).
56. H. Su, W. Zhou, W. Zhou, Y. Li, L. Zheng, H. Zhang, M. Liu, X. Zhang, X. Sun, Y. Xu, F. Hu, J. Zhang, T. Hu, Q. Liu, S. Wei, In-situ spectroscopic observation of dynamic-coupling oxygen on atomically dispersed iridium electrocatalyst for acidic water oxidation. *Nat. Commun.* **12**, 6118 (2021).
57. Z. Shi, J. Li, J. Jiang, Y. Wang, X. Wang, Y. Li, L. Yang, Y. Chu, J. Bai, J. Yang, J. Ni, Y. Wang, L. Zhang, Z. Jiang, C. Liu, J. Ge, W. Xing, Enhanced acidic water oxidation by dynamic migration of oxygen species at the Ir/Nb_2O_{5-x} catalyst/support interfaces. *Angew. Chem. Int. Ed.* **61**, e202212341 (2022).
58. J. Liu, D. Xie, X. Xu, L. Jiang, R. Si, W. Shi, P. Cheng, Reversible formation of coordination bonds in Sn-based metal-organic frameworks for high-performance lithium storage. *Nat. Commun.* **12**, 3131 (2021).
59. M. Desmau, M. A. Alsina, J.-F. Gaillard, XAS study of Sn speciation in toothpaste. *J. Anal. At. Spectrom* **36**, 407–415 (2021).
60. V. A. Saveleva, K. Ebner, L. Ni, G. Smolentsev, D. Klose, A. Zitolo, E. Marelli, J. Li, M. Medarde, O. V. Safonova, M. Nachtegaal, F. Jaouen, U. I. Kramm, T. J. Schmidt, J. Herranz, Potential-induced spin changes in Fe/N/C electrocatalysts assessed by in situ x-ray emission spectroscopy. *Angew. Chem. Int. Ed.* **60**, 11707–11712 (2021).
61. C. Liu, Y. Wu, K. Sun, J. Fang, A. Huang, Y. Pan, W.-C. Cheong, Z. Zhuang, Z. Zhuang, Q. Yuan, H. L. Xin, C. Zhang, J. Zhang, H. Xiao, C. Chen, Y. Li, Constructing FeN_4/graphitic nitrogen atomic interface for high-efficiency electrochemical CO_2 reduction over a broad potential window. *Chem* **7**, 1297–1307 (2021).
62. J. Chen, Y. Z. Finfrock, Z. Wang, T. K. Sham, Strain and ligand effects in Pt-Ni alloys studied by valence-to-core X-ray emission spectroscopy. *Sci Rep-Uk* **11**, 13698 (2021).
63. L. Chong, J. Wen, J. Kubal, F. G. Sen, J. Zou, J. Greeley, M. Chan, H. Barkholtz, W. Ding, D. J. Liu, Ultralow-loading platinum-cobalt fuel cell catalysts derived from imidazolate frameworks. *Science* **362**, 1276–1281 (2018).
64. B. Ravel, M. Newville, ATHENA, ARTEMIS, HEPHAESTUS: Data analysis for X-ray absorption spectroscopy using IFEFFIT. *J. Synchrotron Radiat.* **12**, 537–541 (2005).
65. G. Kresse, J. Furthmuller, Efficiency of ab-initio total energy calculations for metals and semiconductors using a plane-wave basis set. *Comp. Mater. Sci.* **6**, 15–50 (1996).
66. G. Kresse, J. Furthmuller, Efficient iterative schemes forab initiototal-energy calculations using a plane-wave basis set. *Phys. Rev. B* **54**, 11169–11186 (1996).
67. J. P. Perdew, K. Burke, M. Ernzerhof, Generalized gradient approximation made simple. *Phys. Rev. Lett.* **77**, 3865–3868 (1996).
68. H. J. Monkhorst, J. D. Pack, Special points for Brillouin-zone integrations. *Phys. Rev. B* **13**, 5188–5192 (1976).
69. P. E. Blochl, Projector augmented-wave method. *Phys. Rev., B Condens. Matter* **50**, 17953–17979 (1994).
70. S. Grimme, J. Antony, S. Ehrlich, H. Krieg, A consistent and accurate ab initio parametrization of density functional dispersion correction (DFT-D) for the 94 elements H-Pu. *J. Chem. Phys.* **132**, 154104 (2010).
71. H. Guo, Z. Fang, H. Li, D. Fernandez, G. Henkelman, S. M. Humphrey, G. Yu, Rational design of rhodium-iridium alloy nanoparticles as highly active catalysts for acidic oxygen evolution. *ACS Nano* **13**, 13225–13234 (2019).
72. G. Meng, W. Sun, A. A. Mon, X. Wu, L. Xia, A. Han, Y. Wang, Z. Zhuang, J. Liu, D. Wang, Y. Li, Strain regulation to optimize the acidic water oxidation performance of atomic-layer IrO_x. *Adv. Mater.* **31**, e1903616 (2019).
73. F.-F. Zhang, C.-Q. Cheng, J.-Q. Wang, L. Shang, Y. Feng, Y. Zhang, J. Mao, Q.-J. Guo, Y.-M. Xie, C.-K. Dong, Y.-H. Cheng, H. Liu, X.-W. Du, Iridium oxide modified with silver single atom for boosting oxygen evolution reaction in acidic media. *ACS Energy Lett.* **6**, 1588–1595 (2021).
74. F. Luo, H. Hu, X. Zhao, Z. Yang, Q. Zhang, J. Xu, T. Kaneko, Y. Yoshida, C. Zhu, W. Cai, Robust and stable acidic overall water splitting on Ir single atoms. *Nano Lett.* **20**, 2120–2128 (2020).
75. O. Diaz-Morales, S. Raaijman, R. Kortlever, P. J. Kooyman, T. Wezendonk, J. Gascon, W. T. Fu, M. T. Koper, Iridium-based double perovskites for efficient water oxidation in acid media. *Nat. Commun.* **7**, 12363 (2016).
76. S. Kumari, B. P. Ajayi, B. Kumar, J. B. Jasinski, M. K. Sunkara, J. M. Spurgeon, A low-noble-metal $W_{1-x}Ir_xO_{3-\delta}$ water oxidation electrocatalyst for acidic media via rapid plasma synthesis. *Energ. Environ. Sci.* **10**, 2432–2440 (2017).
77. Y. Pi, N. Zhang, S. Guo, J. Guo, X. Huang, Ultrathin laminar Ir superstructure as highly efficient oxygen evolution electrocatalyst in broad pH range. *Nano Lett.* **16**, 4424–4430 (2016).
78. Y. Zhao, M. Luo, S. Chu, M. Peng, B. Liu, Q. Wu, P. Liu, F. M. F. de Groot, Y. Tan, 3D nanoporous iridium-based alloy microwires for efficient oxygen evolution in acidic media. *Nano Energy* **59**, 146–153 (2019).
79. J. Lim, D. Park, S. S. Jeon, C. W. Roh, J. Choi, D. Yoon, M. Park, H. Jung, H. Lee, Ultrathin IrO_2 nanoneedles for electrochemical water oxidation. *Adv. Funct. Mater.* **28**, 1704796 (2018).

80. J. Park, Y. J. Sa, H. Baik, T. Kwon, S. H. Joo, K. Lee, Iridium-based multimetallic nanoframe@nanoframe structure: An efficient and robust electrocatalyst toward oxygen evolution reaction. *ACS Nano* **11**, 5500–5509 (2017).
81. L. Yang, G. Yu, X. Ai, W. Yan, H. Duan, W. Chen, X. Li, T. Wang, C. Zhang, X. Huang, J. S. Chen, X. Zou, Efficient oxygen evolution electrocatalysis in acid by a perovskite with face-sharing IrO_6 octahedral dimers. *Nat. Commun.* **9**, 5236 (2018).
82. Q. Feng, J. Zou, Y. Wang, Z. Zhao, M. C. Williams, H. Li, H. Wang, Influence of surface oxygen vacancies and ruthenium valence state on the catalysis of pyrochlore oxides. *ACS Appl. Mater. Interfaces* **12**, 4520–4530 (2020).
83. L. Wang, V. A. Saveleva, S. Zafeiratos, E. R. Savinova, P. Lettenmeier, P. Gazdzicki, A. S. Gago, K. A. Friedrich, Highly active anode electrocatalysts derived from electrochemical leaching of Ru from metallic $_{Ir\ 0.7\ Ru\ 0.3}$ for proton exchange membrane electrolyzers. *Nano Energy* **34**, 385–391 (2017).
84. W. Xu, K. Scott, The effects of ionomer content on PEM water electrolyser membrane electrode assembly performance. *Int. J. Hydrogen Energy* **35**, 12029–12037 (2010).
85. G. Jiang, H. Yu, J. Hao, J. Chi, Z. Fan, D. Yao, B. Qin, Z. Shao, An effective oxygen electrode based on $Ir_{0.6}Sn_{0.4}O_2$ for PEM water electrolyzers. *J. Energy Chem.* **39**, 23–28 (2019).
86. A. Marshall, B. Børresen, G. Hagen, M. Tsypkin, R. Tunold, Electrochemical characterisation of $Ir_xSn_{1-x}O_2$ powders as oxygen evolution electrocatalysts. *Electrochim. Acta* **51**, 3161–3167 (2006).
87. J. Cheng, H. Zhang, G. Chen, Y. Zhang, Study of $Ir_xRu_{1-x}O_2$ oxides as anodic electrocatalysts for solid polymer electrolyte water electrolysis. *Electrochim. Acta* **54**, 6250–6256 (2009).
88. C. Xu, L. Ma, J. Li, W. Zhao, Z. Gan, Synthesis and characterization of novel high-performance composite electrocatalysts for the oxygen evolution in solid polymer electrolyte (SPE) water electrolysis. *Int. J. Hydrogen Energy* **37**, 2985–2992 (2012).
89. E. Rasten, G. Hagen, R. Tunold, Electrocatalysis in water electrolysis with solid polymer electrolyte. *Electrochim. Acta* **48**, 3945–3952 (2003).

Acknowledgments: We thank the BL14W1 station in the SSRF, and the 1W1B station in the BSRF for help with XAS characterizations. The XES beam time was granted by the 4W1B beamline of BSRF. The staff members of the beamline stations are acknowledged for great support in measurements and data collection. We also acknowledge T. Silver for critical reading of this paper. **Funding:** This work was supported by the National Natural Science Foundation of China (grant nos. 92261119 and 22171157), the National Key R&D Program of China (2018YFA0702003), the Beijing Natural Science Foundation (2224096), the Natural Science Foundation of Zhejiang Province (LZ22B030006), the Australian Research Council Discovery Project (DP210102215), and the China Postdoctoral Science Foundation (2021M690086 and 2021TQ0170). X.Z. acknowledges funding support from the Office of China Postdoctoral Council (YJ20200277) and the "Shuimu Tsinghua Scholar Program (2020SM109)" of Tsinghua University, China. **Author contributions:** Y.L., D.W., and W.S. conceived the idea, designed the experiments, planned synthesis, supervised the project, and revised the manuscript. X.Z. conceived the idea, designed the experiments, performed catalyst synthesis and electrochemical measurements, analyzed the characterization results, and wrote the manuscript. J.Y. conducted the DFT calculations and helped with the analysis of obtained results. P.L., Q.W., J.W., E.Z., S.C., Z.Z., W.L., and S.D. helped with the data analysis and article revisions. All authors discussed the results, drew conclusions, and commented on the manuscript. **Competing interests:** The authors declare they have no competing interest. **Data and materials availability:** All data needed to evaluate the conclusions in the paper are present in the paper and/or the Supplementary Materials: TEM and HAADF/ABF-STEM images, EDS analysis, XRD and XPS analysis, electrochemistry, XAS and XES analysis, and DFT computations.

Submitted 18 May 2023
Accepted 13 September 2023
Published 18 October 2023
10.1126/sciadv.adi8025